RESEARCH ARTICLE

Nancy K. Adams · Bruce F. Houghton · Wes Hildreth

Abrupt transitions during sustained explosive eruptions: examples from the 1912 eruption of Novarupta, Alaska

Abstract Plinian/ignimbrite activity stopped briefly and abruptly 16 and 45 h after commencement of the 1912 Novarupta eruption defining three episodes of explosive volcanism before finally giving way after 60 h to effusion of lava domes. We focus here on the processes leading to the termination of the second and third of these three episodes. Early erupted pumice from both episodes show a very similar range in bulk vesicularity, but the modal values markedly decrease and the vesicularity range widens toward the end of Episode III. Clasts erupted at the end of each episode represent textural extremes; at the end of Episode II, clasts have very thin glass walls and a predominance of large bubbles, whereas at the end of Episode III, clasts have thick interstices and more small bubbles. Quantitatively, all clasts have very similar vesicle size distributions which show a division in the bubble population at 30 μm vesicle diameter and cumulative number densities ranging from 10^7–10^9 cm^{-3}. Patterns seen in histograms of volume fraction and the trends in the vesicle size data can be explained by coalescence signatures superimposed on an interval of prolonged nucleation and free growth of bubbles. Compared to experimental data for bubble growth in silicic melts, the high 1912 number densities suggest homogeneous nucleation was a significant if not dominant mechanism of bubble nucleation in the dacitic magma. The most distinct clast populations occurred toward the end of Plinian activity preceding effusive dome growth. Distributions skewed toward small sizes, thick walls, and teardrop vesicle shapes are indicative of bubble wall collapse marking maturation of the melt and onset of processes of outgassing. The data suggest that the superficially similar pauses in the 1912 eruption which marked the ends of episodes II and III had very different causes. Through Episode III, the trend in vesicle size data reflects a progressive shift in the degassing process from rapid magma ascent and coupled gas exsolution to slower ascent with partial open-system outgassing as a precursor to effusive dome growth. No such trend is visible in the Episode II clast assemblages; we suggest that external changes involving failure of the conduit/vent walls are more likely to have effected the break in explosive activity at 45 h.

N. K. Adams (✉) · B. F. Houghton
Department of Geology and Geophysics, SOEST,
University of Hawaii,
1680 East-West Road,
Honolulu, HI 96822, USA
e-mail: nanadams@soest.hawaii.edu
Tel.: +1-808-9562561
Fax: +1-808-9555512

W. Hildreth
Volcano Hazards Program,
US Geological Survey,
Mailstop 910, 345 Middlefield Road,
Menlo Park, CA 94025, USA

Introduction

While the steady-state behavior of sustained eruption plumes has been adequately modeled (Sparks 1986; Woods 1988; Bursik et al. 1992; Sparks et al. 1992; Koyaguchi 1994; Ernst et al. 1996; Sparks et al. 1997), sudden pauses and abrupt unidirectional shifts in eruptive regime and intensity (e.g., Self and Rampino 1981; Sigurdsson et al. 1984; Self 1992; Paladio-Melosantos et al. 1995; Cioni et al. 1999; Rosi et al. 2001) remain poorly explained. In many theoretical models of large eruptions, thresholds in mass eruption rates (MER) drive first-order shifts in regime, i.e., changes from effusive to explosive eruption (Jaupart and Allegre 1991) or from convecting to collapsing columns (Melnik 2000). In nature, transitions in eruptive style and intensity are complex, sometimes involving pulsatory behavior (e.g., Carey et al. 1990; Rosi et al. 2001; Kokelaar 2002; Druitt et al. 2002), or simultaneous production of convecting columns and pyroclastic density currents (e.g., Wilson and Walker 1985; Fierstein and Hildreth 1992). The

complexity observed in natural systems highlights the need to identify the parameters controlling eruption processes and understanding the interplay between processes.

Eruption dynamics are influenced by processes occurring in (1) the region of magma storage, (2) the volcanic conduit, and (3) the vent. The latter two environments are of interest in this study. In the conduit, magma ascent induces changes in melt rheology during degassing and crystallization (Cas and Wright 1987; Jaupart and Tait 1994; Cashman et al. 2000). Flow dynamics are critically related to melt rheology which will alter in response to changing concentrations of dissolved volatiles, bubbles, and microlites in the melt (Pinkerton and Stevenson 1992; Hess and Dingwell 1996; Manga et al. 1998; Rust et al. 2003). Conduit and vent geometries also have a strong influence on eruption dynamics, particularly on ascent velocity and eruption regime (Wilson et al. 1980; Bursik and Woods 1991; Jaupart and Tait 1994; Woods and Bower 1995). Steady removal of wall rock into intense but stable Plinian plumes can lead to systematic vent enlargement (Carey and Sigurdsson 1989) and column collapse (Francis 1993).

In this study, we examine in detail two of three major breaks in the largest eruption of the 20th century, the 60-h-long Novarupta 1912 eruption (Fierstein and Hildreth 1992; Hildreth and Fierstein 2000). Our study focuses on changes occurring in-and-to the volcanic conduit and vent during Plinian episodes II and III. This eruption is an excellent case study for examining conduit dynamics and evolving vent geometry during a major explosive event because the changing eruptive styles and breaks in activity are readily identifiable in its voluminous deposits. General questions concerning pauses and breaks in otherwise sustained Plinian eruptions can thus be addressed at Novarupta. Why did explosive volcanism pause at the ends of episodes I and II, and what mechanisms drove the final transition to effusive volcanism after Episode III? What was the nature of the degassing? How did processes occurring in the conduit affect the steadiness of the eruption, i.e., what were they and how could they have caused the pulses in intensity? By studying individual pyroclasts from the eruption and quantifying textures, we address such questions.

Background

Eruption description

The 1912 eruption at Novarupta, Alaska is a valuable case study because: (1) it was the most voluminous eruption of the twentieth century (exceeded by only four eruptions in the last 1,000 years); (2) caldera collapse occurred 10 km from vent preserving the very near-vent products of the eruption; and (3) the eruption products have a very wide compositional range (50.4–77.7% SiO_2) defining a chemical stratigraphy which enables correlation of coeval products of highly varying character at widely spaced localities (Fierstein and Hildreth 1992). The 60-h explosive phase of the eruption began 6 June and included, at its peak of intensity, simultaneous deposition of Plinian fall deposits and voluminous ignimbrites (Hildreth 1983, 1987, 1991; Fierstein and Hildreth 1992; Hildreth and Fierstein 2000). Stratigraphy and eyewitness accounts point to two short breaks in the 60 h of Plinian activity at Novarupta on the morning of 7 June and the evening of 8 June, defining three episodes of explosive eruption (Fig. 1). Volumetrically, most of the ignimbrite generation occurred during Episode I; deposition during episodes II–III was dominantly Plinian fall. Explosive volcanism was followed by two episodes of dome/plug emplacement of first dacitic (Episode IV) then rhyolitic (Episode V) composition. Three concentric, nested features define the Novarupta vent region: the crater, the ejecta ring, and the dome (Fig. 2).

Episode II/III stratigraphy

The medial-distal Plinian fall deposits are divided into 8 layers (A–H) by Curtis (1968) formed during three Plinian episodes (I–III) separated by breaks of a few hours (Hildreth 1983; Fig. 1). Episodes II and III, the focus of this study, deposited Plinian falls C-D, and F-G, respectively, with only minor intraplinian pyroclastic flows and surges. The ejecta has a predominantly dacitic composition (Fierstein and Hildreth 1992). These medial-distal falls are classical Plinian deposits in the sense of both Walker (1973) and Pyle (1989) with inferred column heights of 25

Fig. 1 Plot showing the relative amounts of rhyolite, dacite, and andesite erupted with time, modified after Hildreth and Fierstein (2000)
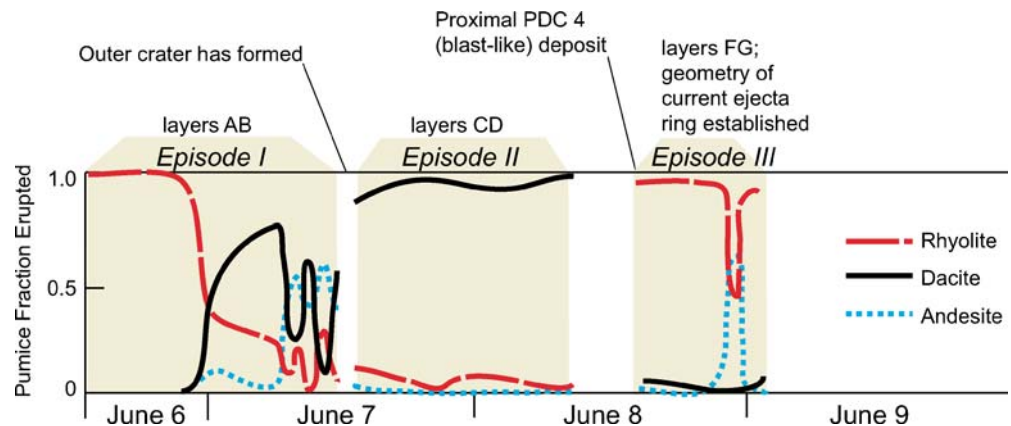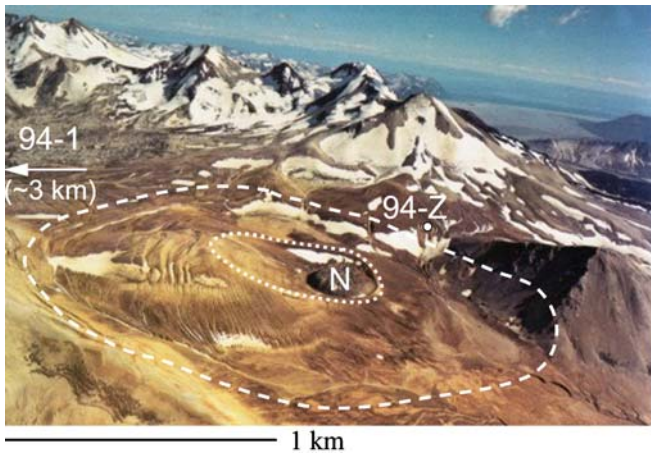
Fig. 2 Aerial photo in the ESE perspective of the near vent region. Three concentric, nested features include the dome (*N*), the ejecta ring (*dotted line*), and the outer crater (*dashed line*); sample sites 94-1 and 94-Z also labeled. Photo courtesy of Hildreth

(CD) and 23 (FG) km (method of Carey and Sparks 1986) and estimated peak mass eruption rates (Fierstein and Hildreth 1992) of 0.6 and 0.4×10^8 kg/s (after Carey and Sparks 1986; Sparks 1986) or 1–2 and 0.2–0.3×10^8 kg/s (after Wilson and Walker 1987). They were followed by deposition of fine ash layers E and H, respectively; broadly synchronous with Layer E in the proximal region is a blast-like pyroclastic density current marking the initiation of Episode III (Houghton et al. 2004). A more complex proximal stratigraphy was established by Houghton et al. (2004) who show that the proximal succession for episodes II and III includes alternations and mixtures of both locally and regionally dispersed fall ejecta as well as thin deposits

of pyroclastic density currents (PDCs) with no regional analogs.

Melt properties and storage

Phenocryst content in the Novarupta high-silica rhyolite (77–78 wt% SiO_2) is 1–3 wt%, whereas the dacites (63–68 wt% SiO_2) and andesites (58–63 wt% SiO_2) contain 30–50 wt% phenocrysts (Hildreth and Fierstein 2000). Phenocrysts in the rhyolites include plagioclase, quartz, pyroxene, and magnetite; with the exception of quartz, a similar assemblage is present in the intermediate magmas. Based on FTIR spectroscopic analysis of melt inclusions trapped in quartz phenocrysts in Episode I rhyolitic ejecta, dissolved H_2O concentrations range from 3.5–4.7 wt% (Lowenstern 1993). Dissolved H_2O ranges between 2.2–3.1 wt% in melt inclusions from plagioclase phenocrysts from Episode II dacitic pumice, and CO_2 in both rhyolites and dacites falls below the minimum detection limit of 50 ppm (Lowenstern 1993).

While debate continues concerning the storage region for the 1912 rhyolite (Hammer et al. 2002), all authors agree the dacite erupted in episodes II and III was stored in a shallow reservoir beneath Mount Katmai 10 km east of Novarupta (Hildreth 1987; Fierstein and Hildreth 1992; Hildreth and Fierstein 2000; Coombs and Gardner 2001; Hammer et al. 2002). Using water-saturated experiments on pumice, Coombs and Gardner (2001) calculated that this rhyolitic magma chamber was located at a depth of 1.8–4.4 km. Hammer et al. (2002) determined for a continuum of intermediate magmas (dacite to andesite) a storage depth of 2–4 km, if they were undersaturated with

Fig. 3 Stratigraphic logs at two sites sampled (*right*) and analyzed during the current study; *red-filled circles* represent samples collected for density measurements (50–100 clasts) and number indicates samples from which individual clasts were selected for image analysis. 94-Z consists entirely of Episode III layers F and G. Photos of the two samples sites (*left*); Novarupta dome is in the background at 94-Z
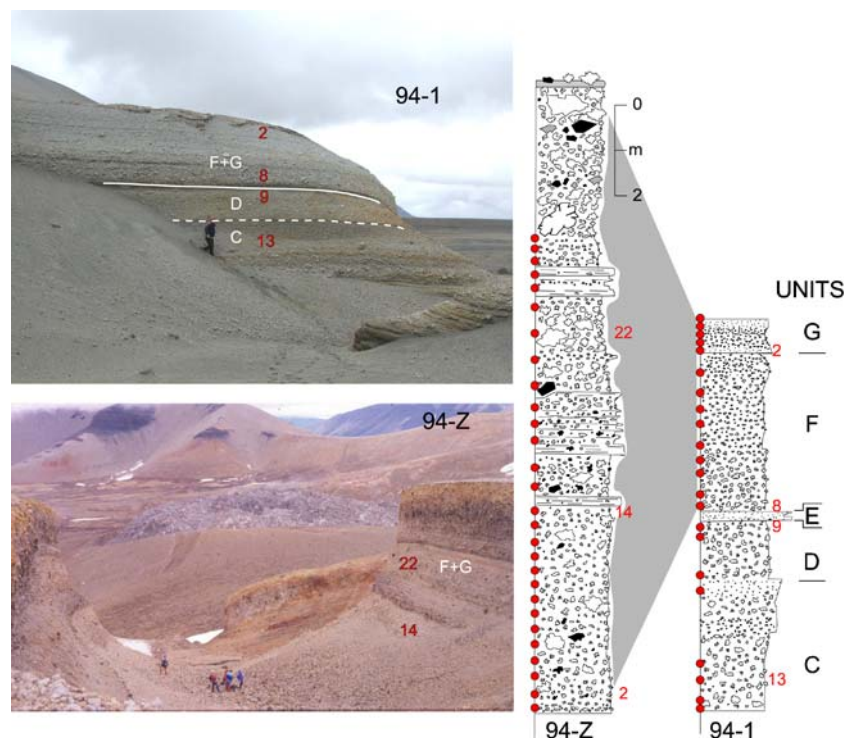
respect to H_2O either because a vapor phase did not exist or because CO_2 was a significant component. Equilibration pressures for the H_2O-undersaturated magmas are 50–75 MPa. If the magmas were H_2O saturated, the depths range from 3–4 km for andesites and 1–2 km for dacites with corresponding pressures of 75–100 MPa and 25–50 MPa, respectively (Hammer et al. 2002).

Techniques

Sample collection

Suites of samples of dacitic pumices were assembled from two key sections within 4 km of the Novarupta vent (sites 94–1 and 94-Z, Fig. 2). To insure representation of the complete range of vesicles sizes and overall vesicularity, each sample contained 50–100 clasts of 16–32 mm diameter following Houghton and Wilson (1989). The vertical sampling intervals were small, typically 2–3 clasts high, and chosen as typical of each eruption layer and spanning the transitions between episodes and the shifts in style/intensity. Samples from these two sites were used to represent the fall layers from episodes II and III, namely layers C, D, F, and G (Fig. 3). At site 94-1, 4 km northeast of the Novarupta vent, the fall sequence of layers C through G is well exposed although G is cut by an erosion surface. However, 800 m south of the vent a more complete G is exposed in a canyon at site 94-Z. The stratigraphy at 94-Z and other proximal sites is more complex than site 94-1 and includes the locally dispersed fall and PDC deposits described by Houghton et al. (2004).

Twenty-two samples totaling ~1,400 pumice clasts were collected from the episode II and III deposits exposed at site 94-1: five from Layer C, three from D, and 14 from F+G. Twenty-three samples were collected from the 94-Z Plinian deposits: 14 from F and 9 from G. In addition, five samples were collected from the deposits of intraplinian PDCs at 94-Z (Fig. 3).

Density/vesicularity

Density measurements were made on each clast from the samples collected at sites 94-1 and 94-Z by the method of Houghton and Wilson (1989). Bulk vesicularity for each clast was then determined using a dense rock equivalent (DRE) density of 2,450 kg/m (Spera 2000).

The patterns of clast density/vesicularity across the stratigraphy were used to select a small number of samples from sites 94-1 and 94-Z for measurements of vesicle size (Fig. 3; Table 1). Samples 13, 9, 8, and 2 were chosen from site 94-1 to represent layers C, D, F, and G, respectively. Samples 2, 14, and 22 were used to analyze clasts from the complex proximal deposits coeval with layers F and G at site 94-Z.

Table 1 Parameters for representative samples

Eruptive episode	Depositional unit	Sampling site	Sample No.-clast No.	Density (kg/m^3)	Ves. (%)	$N_{A\ total}$ (cm^{-2})	$N_{V\ total}$ (cm^{-3})	$N^m_{V\ total}$ (cm^{-3})	n (no./cm^3/cm)	Size range (μm)	Median (μm)	No. included
III	G	94–01	2–5	1,020	58.3	3.8E+05	5.5E+08	2.1E+09	4.4E+12	4–1,989	44	2,772
		94–01	2–16	850	65.4	1.7E+05	1.1E+08	3.8E+08	4.5E+11	8–2,504	59	1,318
		94-Z	22–8	1,180	51.7	2.3E+05	2.8E+08	6.3E+08	2.0E+12	4–1,255	45	1,875
		94-Z	22–24	890	63.5	3.3E+05	4.2E+08	1.2E+09	3.1E+12	4–1,989	54	2,733
		94-Z	22–28	610	75.2	1.2E+05	7.7E+07	2.8E+08	2.9E+11	8–1,580	74	2,817
III	F	94-01	8–9	680	72.2	2.8E+05	4.0E+08	1.2E+09	3.1E+12	4–3,968	61	2,762
		94-Z	14–3	830	66.0	2.6E+05	3.5E+08	1.3E+09	2.7E+12	4–3,152	62	3,824
		94-Z	2–4	810	67.0	3.6E+05	5.5E+08	2.0E+09	4.4E+12	4–1,989	58	2,553
II	D	94-01	9–25	640	74.0	2.1E+05	2.6E+08	9.6E+08	1.9E+12	4–3,152	99	2,315
II	C	94-01	13–55	650	73.4	1.6E+05	1.0E+08	4.3E+08	4.2E+11	8–3,152	75	2,220

DRE value of 2,450 kg/m^3 was used to calculate vesicularities (*Ves.*); $N_{A\ total}$ areal number density of vesicles; $N_{V\ total}$ volumetric number density of vesicles referenced to whole clast; $N^m_{V\ total}$ volumetric number density of vesicles referenced to melt only; n population number density

Image analysis

Textures of pyroclasts, specifically vesicle size distribution, vesicle shape, and abundance of microlites, can be quantified from image analysis and used to study conduit processes (Cashman and Mangan 1994; Mangan and Cashman 1996; Hammer et al. 1999). Scanning electron microscope (SEM) and scanned images from polished thin sections were used to quantify textural features in pumices from individual stratigraphic levels and to measure changes in vesicularity and crystallinity during the major shifts in eruptive intensity at Novarupta. Vesicle size distributions (VSDs) are a tool to constrain the relative timing of bubble nucleation, growth, coalescence, and potentially collapse in explosive eruptions and to understand how the style, timing, and extent of magma degassing influences ensuing eruptive behavior (Mangan et al. 1993; Cashman and Mangan 1994; Polacci et al. 2003). Vesicle shape also preserves information about the state of stress in the magma at the time of quenching (Marti et al. 1999). Theory developed for the interpretation of crystal size distributions (Cashman and Marsh 1988; Marsh 1988; Cashman 1992) has also been applied to vesicle populations (Toramaru 1990; Cashman and Mangan 1994; Klug and Cashman 1994; Mangan and Cashman 1996). Kinetic information about bubble nucleation and growth, which may depend on eruptive parameters such as ascent velocity or radial position in the conduit and on pre-eruptive parameters such as melt temperature and volatile content, can be determined from the VSDs if, as at Novarupta, independent assessments of the appropriate time scales are available. For many samples, VSDs do not follow linear trends describing steady state nucleation and growth but instead indicate more complex histories of magma ascent and degassing.

A subset of 3–6 pumice clasts from each of the chosen samples was selected for image collection and analysis in thin section. Selection was based on the density data and qualitative observations of all the clasts in a sample. Heterogeneity in vesicle size and shape in a single thin-section necessitated that images at four different magnifications were captured and analyzed. The data were then combined in order to completely characterize vesicle size distribution. For Novarupta dacites, the best combination of magnifications is 4.5×, 25×, 100×, and either 250× or 500×. The lowest magnification (4.5×) images were collected by scanning the thin sections on a Hewlett-Packard flatbed scanner at 1,200 dpi resolution. These were captured in order to include the largest vesicles (2–3 mm) in each 16–32 mm clast. Backscatter electron (BSE) images with a resolution of 254 dpi were collected using a JEOL-5900LV SEM operating at a 20 kV accelerating voltage and 1-nA beam current for the higher magnifications. The strategy used for acquisition of images of higher magnification involved nested sets of images. A minimum of two 25× images were taken, carefully chosen to represent the range of vesicle textures in the entire section. Areas with large phenocrysts or high crystal number densities were therefore avoided. Within each of the 25× images, two 100× images were collected, and within each

of the 100×, two images of either 250× or 500× were captured. Thus, a minimum of eight 250× or 500× images, four 100× images, and two 25× images were captured per clast. The decision between collecting images at 250× or 500× was based on the size and number density of the smallest-sized vesicles. Lower limits for the size of measured vesicles were 8 and 4 μm for 250× and 500× images, respectively, using a 20 pixel cutoff value.

Images were processed and analyzed using Adobe Photoshop and Scion Image software. The images were captured in grayscale and then transformed into binary images in which vesicles are black and glass is white. Manual editing of the images was required to rebuild vesicle walls broken during thin sample preparation and to remove flaws such as air bubbles or grinding compound. In addition, thin bubble walls were often lost during image acquisition or during the conversion from grayscale to binary and had to be redrawn. The final binary images were analyzed with Scion Image software to obtain both the mean grayscale value and individual vesicle measurements of area and shape.

For each vesicle area measured, an equivalent diameter for a circle with the same area was calculated. Based on this diameter, vesicles were binned, and areal number densities (N_A) were calculated for each bin and adjusted for phenocrysts. Specifically, N_A refers to the number of cross sections within a certain size interval per total image area at a particular magnification corrected for vesicles cut by the edge of the image. Conversion from two-dimensional to three-dimensional number densities (N_V), i.e., number of vesicles within a certain size interval per unit volume, was performed based on the method of Sahagian and Proussevitch (1998). The method relies on the intersection probabilities for spheres to determine conversion coefficients (α) for each bin-size. N_V can then be calculated from N_A using (α) and a mean projected height ($\overline{H}$), i.e., typical diameter for vesicles in that bin-size. The result corrects for large vesicles cut at less than their maximum diameter and incorrectly counted in smaller size classes. The volume fraction for each bin-size was calculated using N_V and the volume of a sphere with a diameter equal to $\overline{H}$ and adjusted so that the cumulative volume fraction matched the measured vesicularity. For the Novarupta data, the summed volume fraction is typically ~10% higher than the measured vesicularity and principally reflects uncertainty introduced by the assumption of a spherical geometry for the bubbles. Notwithstanding the non-spherical nature of the large bubbles and their low abundance in the Novarupta samples, this technique remains the only viable alternative for working with such bubble size distributions and, despite these limitations, gives internally consistent results. Given the number of geometric bins (24–28) required to quantify Novarupta vesicle sizes, an expanded scale of α-values (K.V. Cashman, 2002, personal communication) was used. The cumulative number density ($N_{V\ total}$) referenced to the matrix of the clast, i.e., total clast volume less the phenocrysts, and determined by summing the number density for each bin

size (N_V) records the rate and timing of nucleation of vesicles during the rise of a parcel of magma. Cumulative number densities referenced to the melt volume $\left(N_{V\,total}^m\right)$ have also been determined for each clast to allow for the misleading effect of the vesicle population itself on the number density (Klug et al. 2002).

Results

Density

Samples from site 94-1 show most clearly the pattern of changing clast density with time through episodes II and III. Episode II data are remarkably consistent; although densities range from 350–1,030 kg/m³ for the eight samples (Fig. 4), the mean density of samples only increases slightly from the start to the finish of the episode, rising from 630 to 660 kg/m³. In contrast, mean density increases gradually but significantly with stratigraphic height in the 14 samples spanning Episode III; the sample representing the close of the episode has a mean density of 900 kg/m³.

Pumices collected from Episode III fall deposits at site 94-Z have densities ranging from 410–1,570 kg/m³ with mean values between 740–880 kg/m³. When comparing the density distributions from 94-1 and 94-Z samples, the proximal pumices consistently have slightly higher modal

densities than those at more distal site 94-1 (Fig. 5), reflecting a very mild role of density fractionation in the Novarupta plumes with distance from source (cf., Houghton and Wilson 1989).

Based on their densities, clasts from within seven samples representing the episodes II and III eruptive sequence were selected for image analysis. One clast with modal density for each sample was thin sectioned and measured. From site 94-1, clasts from samples 2, 8, 9, and 13 (layers G–C, Fig. 5) were used. The measured density for each of these clasts was 850, 680, 640 and 650 kg/m³, respectively. Characterizing the close of Plinian activity more proximally, three clasts from samples 22, 14, and 2 from site 94-Z (layers G and F, Fig. 5) were also examined. The measured densities for the three modal clasts at site 94-Z ranged from 810–890 kg/m³. In both sections (94-1 and 94-Z), the modal densities of Layer G show a progressive

Fig. 5 Histograms showing density distribution for the seven samples examined in this study. *Red bins* represent the density range from which an individual clast was selected for image analysis. In sample 94-Z-22, modal density ranges between 900–1,000 kg/m⁻³, and the mean density for the sample is 880 kg/m⁻³, so the clast used to represent intermediate density had a density of 890 kg/m⁻³. Additional high and low-density clasts were selected from Layer G. Notice the shift in modal values in G. The range of higher modal values for site 94-Z reflects fractionation of fall material with distance from the source
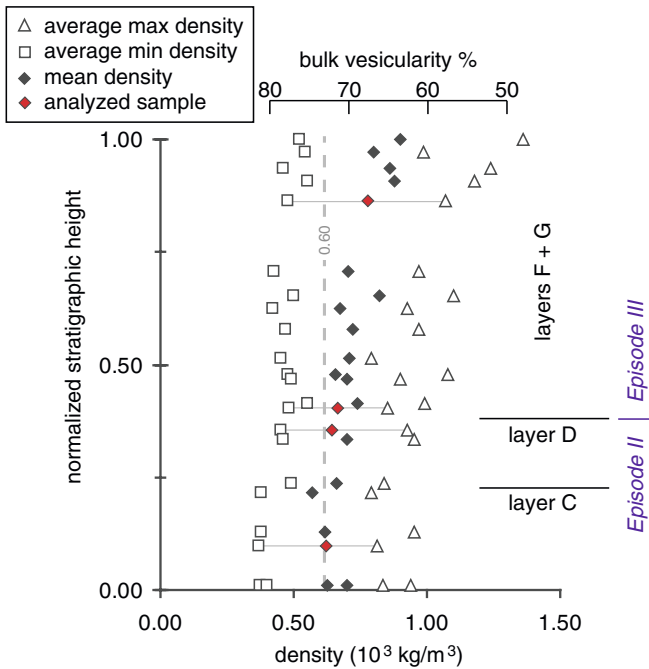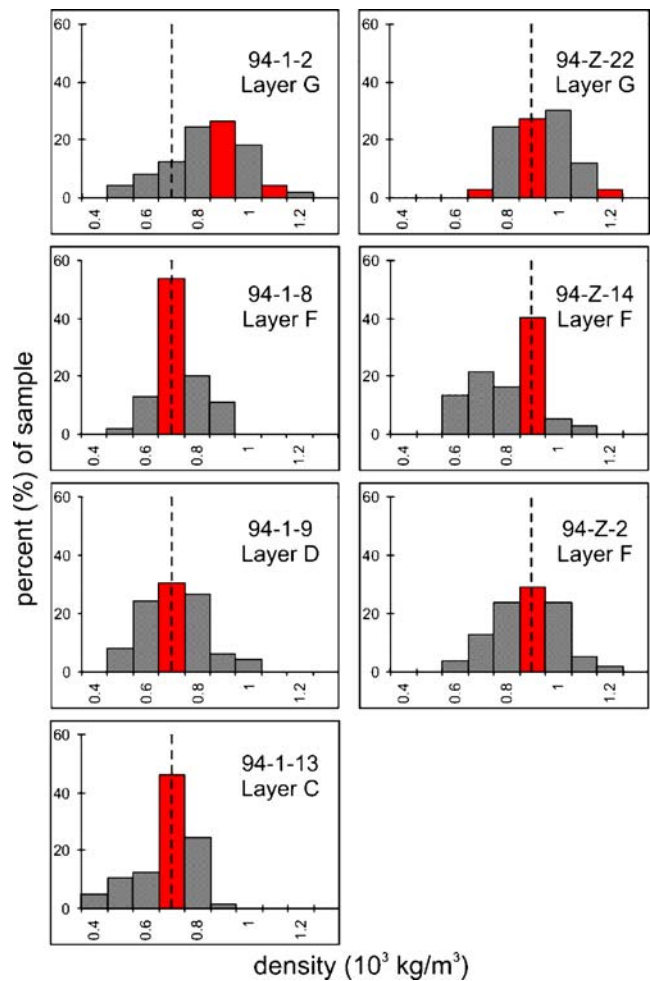

Fig. 4 Low, mean, and high-density values for samples collected at site 94-1 against normalized stratigraphic height. *Open triangles* represent an average of the three maximum density clasts per sample; *open squares* an average of the three minimum density clasts. Samples used during thin section analyses are *shown in red*. Mean density value (*filled diamonds*) increased from Layer C (600 kg/m³, as indicated by the *gray dashed line*) to Layer G (880 kg/m³), i.e., as the eruption progressed

shift away from those of layers C, D, and F (Figs. 4 and 5). To better determine the processes that might be causing the increase, additional clasts were selected representing high and low-density extremes in two samples: 94-1-2 (high density 1,020 kg/m^3), 94-Z-22 (high density 1,180 kg/m^3 and low density 610 kg/m^3).

Qualitative observations of vesicles

Diverse textural features characterize the pumices in thin section (Fig. 6). Some clasts show uniform distribution of a range of vesicle sizes throughout the slide (Fig. 6a). However, other ubiquitously heterogeneous clasts show distinct regions where small bubbles (diameters ≤5−25 μm) predominate and are surrounded by a matrix of mid-to-coarse vesicles (75–100 μm and ≥175 μm diameters,

respectively; Fig. 6b). Independent of the degree of heterogeneity, a marked predominance of intermediate-to-coarse bubbles is conspicuous within some slides (Fig. 6c). Bubble deformation is present in some pumices and typically occurs as bands of elongated vesicles crossing larger regions of more equant bubbles (Fig. 6a, b, d). The bands tend to range in width from ~50–500 μm, suggesting the presence of localized shear zones on a range of scales.

Many stages of bubble coalescence are evident in the Novarupta pumices (Fig. 7). The expansion of smaller bubbles into larger bubbles can be seen throughout the eruptive sequence ('donut-like' features of Klug et al. 2002). As in Mazama pumices (Klug et al. 2002), interaction between equally-sized bubbles often results in very thin planar melt films (~1 μm) inferred to be caused by approximately equal pressures acting on the film from inside each bubble. Wrinkling and incomplete retraction of

Fig. 6 Back-scatter electron images (glass *gray-white*, vesicles *black*) captured from clasts from layers *C,D,* and *F* that represent the range of textures present in episode II and III. Rectangular regions on the right-hand images are shown at higher magnification in the left-hand images. **a** Layer F-range of vesicle sizes is evenly distributed; **b** Layer F-regions of smaller vesicles are surrounded by domains of intermediate-coarse vesicles; **c** Layer D-image is dominated by coarser bubbles; **d** Layer C–thin bubble walls are prominent. In **a,b,** and **d,** bands of stretched vesicles cut through regions of more regularly shaped vesicles
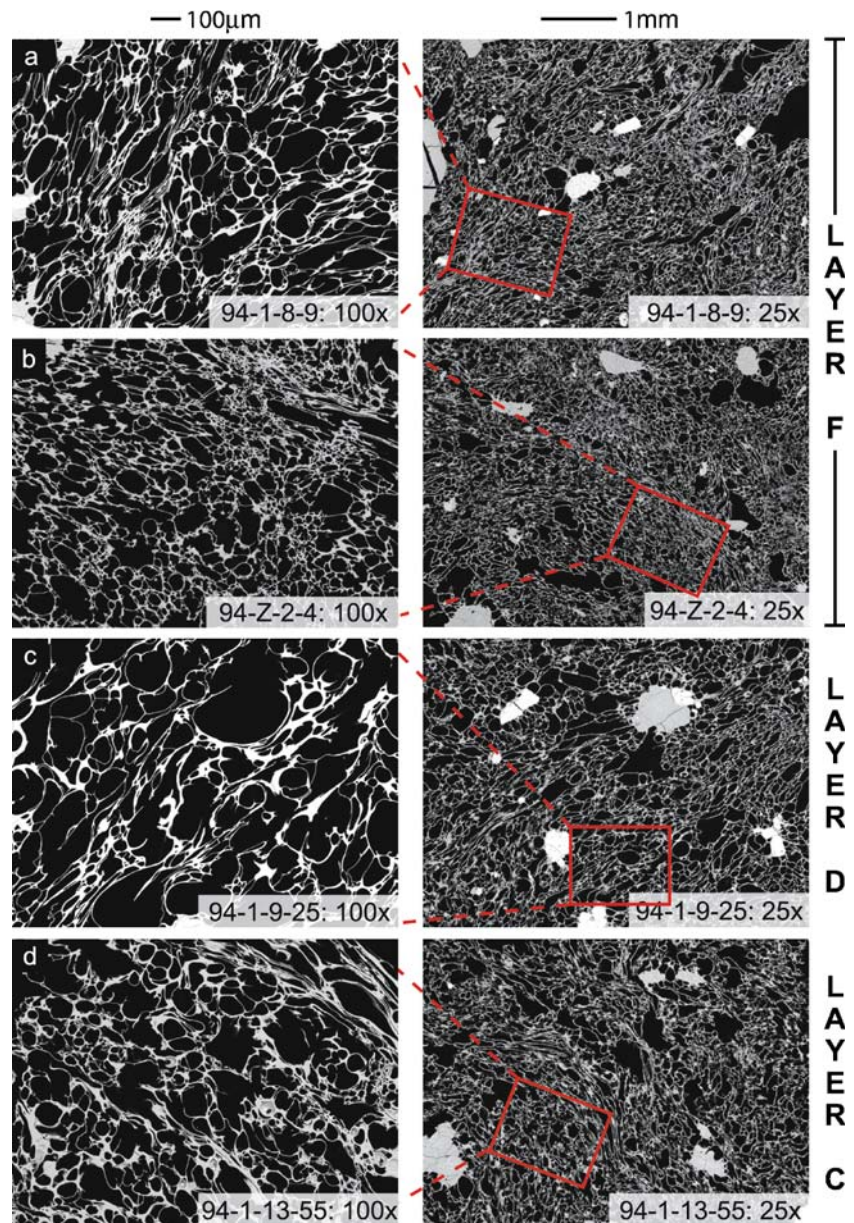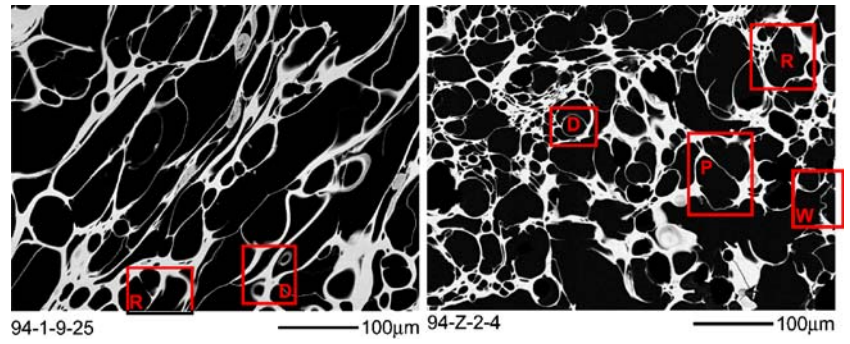
Fig. 7 High magnification images with coalescence features (donuts *D*, wall rupture *R*, wrinkling *W*, planar walls *P*) located within drawn boxes

bubble walls, signs of wall failure as two bubbles coalesce, occur most frequently when medium-to-coarse bubbles interact. Coalescence generally does not occur until melt films thin to ≤ 3 μm in thickness. If wrinkling occurs, the
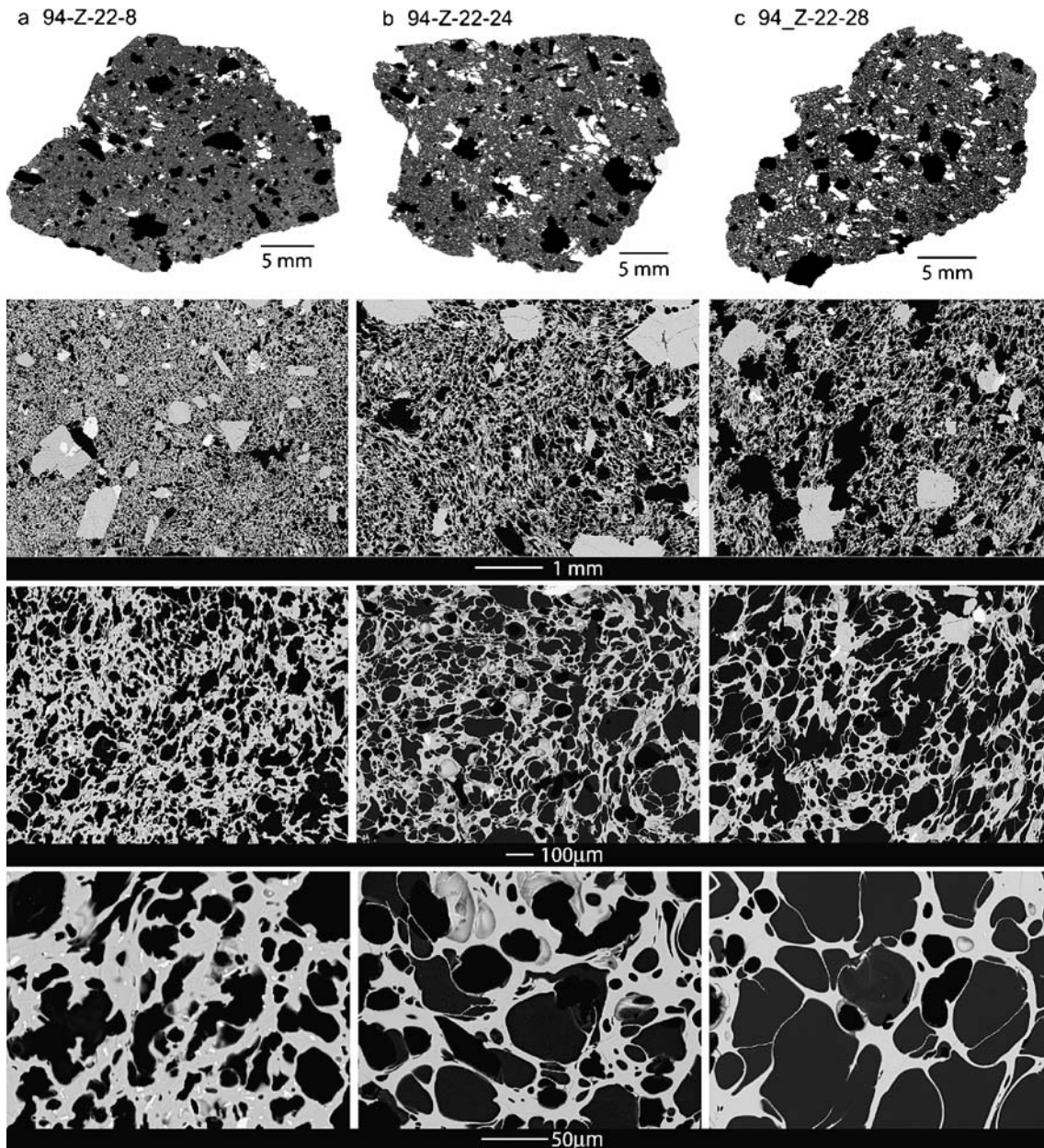

Fig. 8 High, modal, and low-density clasts (**a**–**c**, respectively) from Layer G. All show wall thickening and complex bubble shapes. Note the complex bubble shapes among even the smallest bubbles in the high-density clast (**a**)

thickness of the bubble walls appears to be in the range of 1–3 μm. These parameters on film thicknesses coincide with measurements on the dacites and rhyolites studied by Klug and Cashman (1996). They observed wrinkling inwalls <5 μm thick and rupture at <1 μm thickness. Based on these observations and a comparison between the largest bubbles that can coalesce via film thinning for critical thicknesses of 100, 10, and 0.1 μm (Fig. 7 in Klug and Cashman 1996), they suggest the best estimate for critical wall thickness for dacitic and rhyolitic magma is 1 μm.

Qualitative comparisons among the modal clasts from different stratigraphic levels promote some understanding of changes with time in the processes and conditions in the conduit during the eruption. Despite some bands of elongated vesicles, the distribution of vesicles of all sizes in the modal clast from Layer C (Fig. 6d) is relatively uniform and the vesicle walls appear moderately thin (typically 7–15 μm). Likewise, the modal pumice from Layer D (Fig. 6c) has a very uniform texture, but the vesicles walls are the thinnest of all the examined clasts (typically only 1 μm thick and the average being ~7 μm) and the images are dominated by coarse, coalesced vesicles. Pockets of elongated vesicles between heterogeneous clusters of fine and intermediate-coarse bubbles (Fig. 6a, b) describe pumices from Layer F. Thicker glass walls (typically ~20 μm) and a higher abundance of small vesicles than for the clasts from layers C-F characterize Layer G modal clasts (Fig. 8b); also, bubble elongation occurs in regions, but the regions themselves are not narrow bands as in other clasts. High and low-density clasts were also photographed for Layer G. The low-density clast (Fig. 8c) has some 1–2 μm thick walls but is mostly characterized by intermediate-to-thick interstices (10–25 μm wide) while the modal (Fig. 8b) and the high-density pumices (Fig. 8a) are completely dominated by intermediate (10–15 μm) to thick (15–25 μm) bubble walls. The principal variability in Layer G pumices appears to be in the bubble size distribution; low-density clasts have an even mix of intermediate- and coarse-sized bubbles, modal density clasts have mostly intermediate-sized bubbles with a small population of coarse bubbles, and high-density clasts have a few intermediate-sized bubbles among mostly smaller bubbles. In all clasts, however, complex amoeboid bubble shapes suggest an advanced state of bubble-bubble interaction, e.g., small bubbles in the high-density clast (Fig. 8a). Features such as wall retraction and planar walls demonstrate that coalescence affected the shapes of bubbles in G pumices. The tortured appearance of individual vesicles, as if they have been pinched, also becomes more developed with increasing density.

Quantitative vesicle size data

Vesicle size distributions

Like crystal size distributions (CSDs; Cashman and Marsh 1988; Marsh 1988), vesicle size distributions (VSDs) can be expressed as functions of population density. The vesicle population density n refers to the number of vesicles of each size increment per unit volume and has units of mm^{-4}; it can be determined from the slope of the cumulative number distribution (dN_V/dL) where L is equivalent diameter (mm). Under steady-state conditions, i.e., a balance of vesicles growing into and out of each size range (Cashman and Marsh 1988) where growth rate is independent of vesicle size, a straight line will result when $\ln(n)$ is plotted against L (Mangan and Cashman 1996). The plots of $\ln(n)$ vs. L for the Novarupta dacites, however, show curved trends (Fig. 9) which can be resolved into two segments. Vesicles ≤30 μm plot as steeply sloping straight lines and >30 μm as curves. The profiles are strikingly similar to other samples from Plinian eruptions of silicic magmas, e.g., Mt. Mazama (Klug et al. 2002), Vesuvius AD 79 (Gurioli et al. 2004), 1.8 ka Taupo (Houghton et al. 2003).

Several factors may be influencing the nonlinearity of the VSDs seen in natural systems. Because rates of bubble nucleation and growth are not constant for a decompressing magma during an explosive pyroclastic eruption (Lyakhovsky et al. 1996; Blower et al. 2001b; Klug et al. 2002), the steady-state assumption implicit in CSDs does not apply a priori to all VSDs. In addition to nucleation and unrestricted growth, other processes such as bubble ripening or coalescence affect the linearity of the VSD. Mangan and Cashman (1996) demonstrate that a polymodal bubble distribution, often a signature of coalescence, will produce a segmented VSD in which segment-slope flattens with increasing bubble size. Additional work (Gaonac'h et al. 1996a; Simakin et al. 1999; Mangan et al. 2004) has described VSDs of many different forms, including exponential and power-law relationships.

Vesicle volume distributions

As an alternative to VSDs, plots of vesicle volume distributions (VVDs) can be used to interpret the processes and mechanics that produce more complex textural signatures. The distribution of volume fraction against
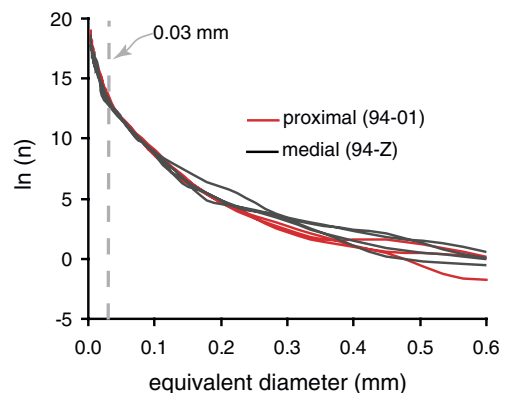

Fig. 9 Natural log of population density (no. of vesicles/mm³/mm) against vesicle size; vesicles <0.03 mm plot as a straight steep line, and >0.03 mm the data are best described as curved
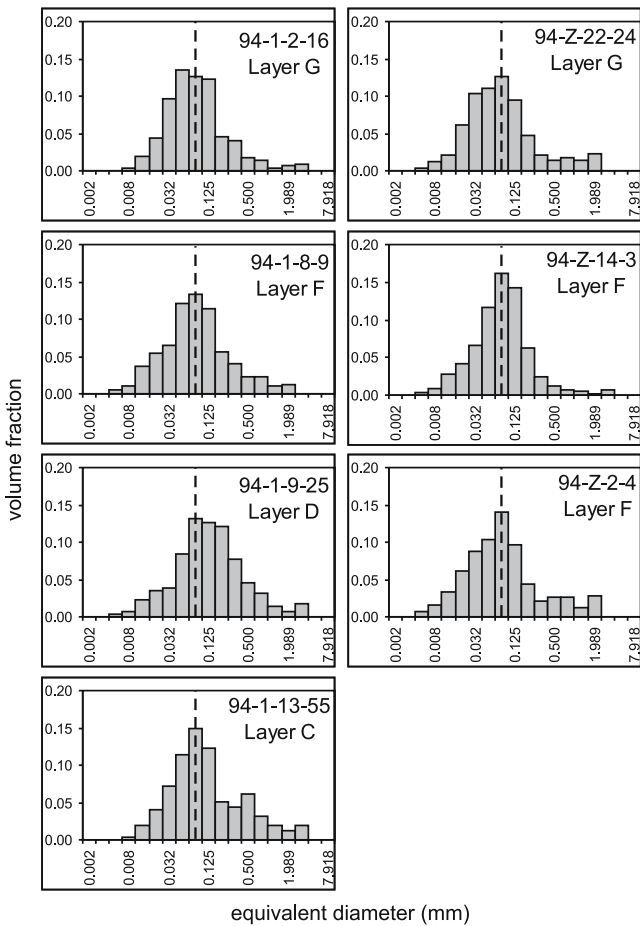
Fig. 10 Histograms showing the distribution of volume fraction against vesicle size for the seven studied modal density clasts. Horizontal scale calculated from minimum vesicle size using a geometric factor $10^{0.1}$ (geometric bin size classes)

vesicle diameter (Fig. 10) can reveal multiple bubble populations and a predominance of small or large vesicles. Median vesicle diameters, also useful when comparing clasts from different fall layers, can be directly determined as the fiftieth percentile on plots of cumulative vesicle volume data versus vesicle diameter size (Fig. 11).

For many Plinian pumice clasts, VVDs are distinctly polymodal (e.g., Sparks and Brazier 1982; Whitham and Sparks 1986; Orsi et al. 1992; Klug and Cashman 1994;

Klug et al. 2002). This is not the case for the 1912 eruption. Subordinate peaks at larger diameters are at best poorly developed in the Novarupta dacites (Fig. 10). Most samples do have, however, a tail of coarse bubbles extending up to 3 mm in equivalent diameter. In addition to the apparent unimodality of the VVDs, the modal size of the bubble population is remarkably consistent at 80 μm. The predominance of a particular vesicle size range, on the other hand, changes throughout the eruption sequence. Layers C and F at site 94-1, both representing sustained activity during the early stages of a Plinian episode, have similar distributions with sharp symmetrical peaks. The two samples of Layer F at site 94-Z have fewer coarse-sized bubbles than F at site 94-1 but still reveal the same general distribution. The mode for Layer D, representing the close of Episode II, is broader and skewed slightly toward coarser sizes. For Layer G (the close of Episode III and final cessation of Plinian activity), the mode for 94-Z is slightly less distinct than the mode for 94-1, but both distributions are skewed toward finer sizes.

The near-unimodal distributions apparent from the volume fraction histograms result in smooth sigmoidal curves with virtually no slope breaks between discrete size populations on plots of cumulative volume fraction versus size (Fig. 11). To compare clasts, layers have been grouped by the stage of Plinian activity they represent; samples from layers C and F represent early sustained activity and layers D and G were deposited towards the close of episodes II and III, respectively. Data from layers C and F show remarkably little variation; for both medial and proximal samples of Layer F, the curves are virtually coincident, especially at their intersection with the fiftieth percentile. The median vesicle size values for Layer F samples (Table 1) range narrowly between 58–62 μm, and the value for Layer C does not deviate greatly from this range (75 μm). Clasts from layers D and G are more variable. The two modal Layer G clasts from 94-1 and 94-Z have very similar forms, not unlike the curves of layers C and F. Median values for modal Layer G are 54 and 59 μm again reminiscent of layers C and F; in comparison the median diameter for the Layer D pumice increases to approximately 100 μm.

High, modal, and low-density clasts from within the same sample can also be compared via cumulative volume

Fig. 11 Cumulative volume percent plot for modal density clasts (*left*) from layers C (*black*) and F (*gray*). Cumulative volume percent plot for modal density clasts (*right*) from layers D (*black*) and G (*gray*). The range of median vesicles sizes is wider between the D and G curves than between the C and F curves
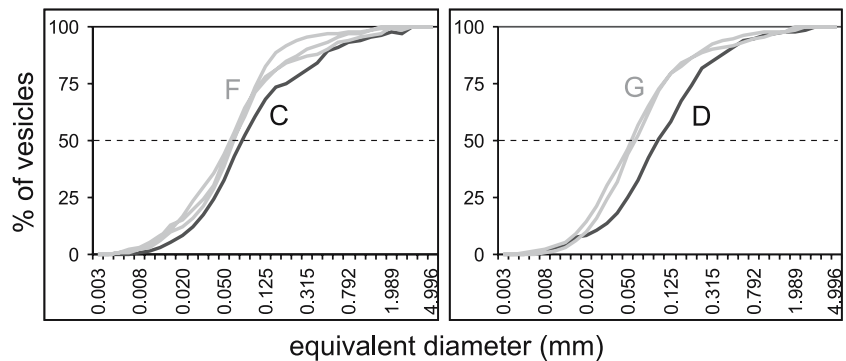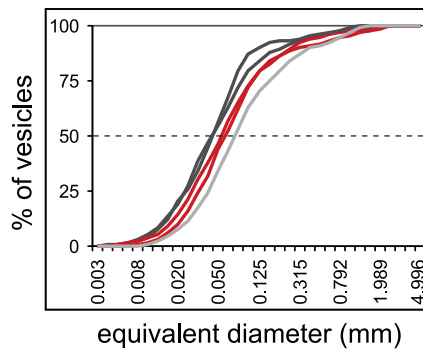
Fig. 12 Cumulative volume percent plot for high, modal, and low-density clasts for Layer G; modal density shown in *red*, high density in *black*, low density in *light gray*

percent plots to examine diversity among clasts erupted simultaneously (Fig. 12). The same pattern emerges for the proximal and medial samples from Layer G. The median value increases from ~60 to ~75 μm from the mode to the low-density clast, respectively, and the value decreases to ~45 μm for the high-density clasts.

Cumulative number densities

Power-law distributions of bubble size typically show linear trends on log-log plots when vesicle number is a function of size (Gaonac'h et al. 1996a,b; Blower et al. 2001a,b); this relationship holds for a wide range of vesicle sizes (>30 μm diameter) in the Novarupta data (Fig. 13). As L approaches the smallest vesicle size measured in the clast, $N_V > L$ approaches the cumulative number density ($N_{V\ total}$) of the clast. When $N_V > L$ is plotted against L on a log-log plot, the trends for all clasts define a best-fit line with a slope of −3.9 (Fig. 13). The linearity starts to collapse at $\log L = 1.5$ (i.e., 30 μm), and an exponential trend better describes the bubbles ≤30 μm. So despite the near-unimodal volume distributions seen on plots of volume fraction versus vesicle size for all the
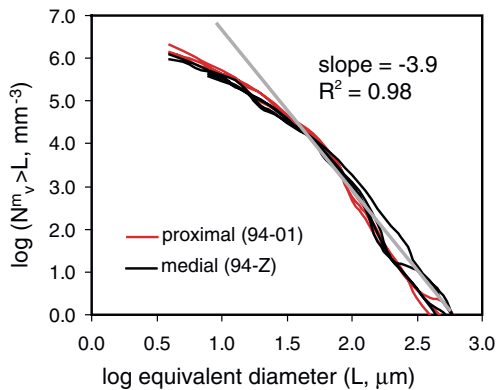

Fig. 13 Number of vesicles greater than a given size (cumulative number density referenced to the melt volume) versus size on a log-log plot. The data are best fit by a straight line (shown in *gray*) with a slope of −3.9 until $\log L = 1.5$ (30 μm); for $\log L < 1.5$ (<30 μm), the data are best described as exponential

samples (Fig. 10), cumulative number densities suggest two size populations of bubbles about a size of 30 μm (the same division as seen on the ln (n)–L plot Fig. 9). The smallest vesicle counted during this study was ~4 μm in diameter, so for consistency with earlier work of Blower et al. (2002) and Klug et al. (2002), the VSD for each sample has been extrapolated to $L = 1$ μm (i.e., $\log L = 0$). The cumulative number density (N_{Vtotal}) for all measured vesicles, i.e., larger than 4 μm, ranged from 7×10^7 cm^{-3} to 5×10^8 cm^{-3} (Table 1). If we fit the trend of bubbles ≤30 μm with an exponential curve and extend this to 1-μm vesicle diameter size, extrapolated cumulative number densities vary from $1–8 \times 10^9$ cm^{-3}. In highly vesicular clasts, cumulative number density ($N_{V\ total}$) calculated based on the volume of the entire clast appears low since much of the volume is in fact comprised of vesicles. Vesicle number densities can also be calculated based on melt volume only $\left(N_V^m\right)$, i.e., corrected for vesicle volume; at 4 μm, cumulative number density values referenced to the melt volume ($N^m_{V\ total}$) range from 2.5×10^8 cm^{-3} to 2×10^9 cm^{-3} (Table 1) and at 1 μm from 2×10^9 cm^{-3} to 2×10^{10} cm^{-3}.

Interpretation

Bubble nucleation

The similarities in bubble number density and size distribution for all the Novarupta pumices are strongly suggestive of similar histories of bubble nucleation and growth for the majority of the melt erupted in 1912, at least during the early stages of ascent in the conduit. Near-unimodal VVDs (Fig. 10) such as those modeled by Toramaru (1989; 1990), suggest that vesiculation occurred over a short time interval at an early stage of decompression with little subsequent nucleation. In experiments on water-saturated high silica rhyolites, Gardner et al. (1999) varied decompression rates and hence levels of supersaturation (ΔP). These experimental runs agreed with Proussevitch and Sahagian (1996; 1998) in that ΔP dropped significantly when porosities reached greater than ~10 vol%. Even at the fastest decompression rates (1.0 MPa/s), only one nucleation event occurred (Gardner et al. 1999). If this were so for the Novarupta melt and the VVDs were created by a single short-lived episode of nucleation and subsequent steady state growth, the expected modes would be narrow and shift to larger values of vesicle diameter with time as seen in experimental samples (Lyakhovsky et al. 1996; Gardner et al. 1999). The Novarupta histogram-VVDs do appear almost Poissonian, however, modes for all pumices are broad, typically 0.05–0.1 mm, and the peak values on the vesicle volume histograms for the modal density clasts do not shift significantly to larger vesicle sizes from Layer C to Layer G (Fig. 10). We suggest nucleation for the 1912 melt was more complex than the scenarios in the afore-mentioned models and experiments. Additional nucleation accompa-

nying mid-stage to late-stage growth of earlier formed bubbles would account for the volume fraction distributions with broad peaks and the significant proportion of small bubbles.

In addition to the timescale over which nucleation occurred, the mechanism of nucleation provides insights into conduit conditions, e.g., rates of decompression and ascent rates. Recent experimental work (Gardner et al. 1999; Mourtada-Bonnefoi and Laporte 1999; Mangan and Sisson 2000) has built on the important study by Hurwitz and Navon (1994) involving bubble nucleation in high silica melts. These studies indicate that large supersaturations (ΔPs) predicted by homogeneous nucleation theory are correct. In the absence of a large number of efficient nucleation sites, onset of nucleation in melt is delayed until shallow levels and degassing is a markedly disequilibrium process. In contrast, during heterogeneous nucleation a large number of potential nucleation sites greatly reduces the supersaturations required to initiate bubble nucleation, and nucleation commences early such that during ascent gas and magma remain approximately in equilibrium. Heterogeneities in melt which serve as nucleation sites include crystals, conduit walls, etc.

Hurwitz and Navon (1994) and Navon and Lyakhovsky (1998) propose that bubble nucleation in most natural silicic systems is controlled by heterogeneities. Conversely, Mangan and Sisson (2000) suggest that crystal number densities, i.e., number of potential nucleation sites, as high as 10^4 cm^{-3} do not prevent supersaturations high enough to trigger homogeneous nucleation. Furthermore, powerful sustained eruptions are actually favored by high degrees of supersaturation, delayed onset of nucleation, and disequilibrium degassing, so homogeneous rather than heterogeneous nucleation should be the dominant mechanism of bubble formation during Plinian eruptions (Mangan and Sisson 2000; Mangan et al. 2004). They concede, however, a combination of both mechanisms probably occurs in most natural systems. The crystallinity, i.e., availability of potential nucleation sites, of the magma as it enters the base of the conduit influences the interplay of the two mechanisms and subsequently equilibrium versus disequilibrium degassing.

Vesicle number densities provide a link between natural samples and experimental data. The 1912 number densities ($N_{V\ total}$ and $N^m_{V\ total}$) range from 10^7–10^9 cm^{-3} (Table 1); experimental results for silicic melts show homogeneous nucleation number densities of 10^7–10^9 cm^{-3} (Mourtada-Bonnefoi and Laporte 1999; Mangan and Sisson 2000) and of 10^6–10^8 cm^{-3} (Hurwitz and Navon 1994; Gardner et al. 1999) for heterogeneous nucleation. In the Hildreth (1983) study, no microlites are seen in the 1912 dacites, but the ejecta are characterized by 30–50% phenocrysts in the ratio plagioclase 5, clinopyroxene 1, and magnetite 1. In the course of our work, only one out of the 11 dacite pumices examined from episodes II–III had microlites, and it was characterized by ~5% plagioclase microlites (Fig. 8a). Thus, two possible scenarios emerge for nucleation conditions at Novarupta: (1) Absence of microlites and a general shortage of efficient nucleation sites lead to a delay in nucleation until extreme supersaturation pressures are reached; (2) Abundance of phenocrysts, despite the dominance of plagioclase (known to be an inefficient nucleation site), triggers bubble nucleation at lower supersaturation pressures.

Experimentally, homogeneous nucleation, a.k.a., scenario (1), in silicic melt is not observed in samples with <5 wt% H_2O and <600 ppm CO_2 unless supersaturations are very high (>120–130 MPa; Mourtada-Bonnefoi and Laporte 1999; Mangan and Sisson 2000). Heterogeneous nucleation can occur with supersaturations on the order of 5 MPa (Hurwitz and Navon 1994). Given the modeled storage depths of 2–4 km for the 1912 intermediate magmas (Hammer et al. 2002), a supersaturation pressure reaching 120 MPa seems implausible. Additionally, the pre-eruptive H_2O content in the Novarupta magma is low compared to saturations in which homogeneous nucleation has been triggered experimentally unless CO_2 was a more significant component than indicated from melt inclusions. Furthermore, experiments by Gardner et al. (1999) and models by Proussevitch and Sahagian (1996; 1998) indicate plausible decompression rates in silicic explosive systems are not consistent with levels of supersaturation high enough to trigger homogeneous nucleation. We acknowledge, however, that experimental setups are restricted to specific modeling conditions; as such, their application to natural settings is limited, and neither homogeneous nor heterogeneous conditions can definitively be dismissed. So while a comparison between conditions at Novarupta, i.e., volatile content and decompression rates, and experimentally determined parameters contradicts the occurrence of homogeneous nucleation, the high number densities and general explosivity of the 1912 eruption suggest high nucleation rates and hence favor homogeneous nucleation (Mangan et al. 2004). We suggest at Novarupta extreme supersaturations were not reached throughout the melt, and heterogeneous and homogeneous nucleation probably operated in combination. This amalgamation was caused by variations in the melt and within its ascent history.

Bubble coalescence

Significant bubble coalescence strongly influences vesicle size and volume distributions. It has two principal effects on the bubble population: (1) the large bubble populations are enhanced at the expense of smaller sizes often generating a bimodal size distribution (Orsi et al. 1992; Cashman and Mangan 1994), and (2) the shapes of the bubbles become more complex. Gaonac'h et al. (1996a) proposed that growth involving cascading coalescence of bubble populations in highly viscous magma produces power-law size distributions. While Blower et al. (2001a; 2002) simulated similar distributions through continuous nucleation, the exponent associated with coalescence distributions was distinguishably higher (~4). Given that the power-law relationship for larger bubbles in the Novarupta pumices is described by an exponent of 3.9 (Fig. 13), we infer coalescence strongly influenced vesicle

growth for bubbles >30 µm. Furthermore, Mangan and Cashman (1996) suggest bubble coalescence produces a curve in which slope flattens with increasing bubble size on a plot of ln (n) vs. diameter. Curves fitting the Novarupta data for bubbles >30 µm in diameter on Fig. 9 are indeed characterized by an increasingly flatter slope. Coalescence is also abundantly evident in the shape of intermediate-to-coarse bubbles in the images (Fig. 7); shapes are complex and strongly deviate from spherical. Toramaru (1988) and Proussevitch et al. (1993) considered critical film thicknesses and thinning rates of films while examining bubble growth and foam stability. During early stages of foam development, bubbles nucleate and grow by diffusion and decompression in an unrestricted fashion defining an exponential size distribution. At this point, coalescence is inhibited by the thickness of the bubble walls. With continued nucleation and growth and hence increasing vesicularity and thinner walls, bubble-bubble interactions and coalescence commences. Klug and Cashman (1996) suggest these interactions begin at ~30% vesicularity, well below the volume fraction of a true foam (74%). So coalescence probably overlapped in time with bubble nucleation and growth during the 1912 eruption. We suggest the onset of coalescence as a significant growth process is manifested in the VSD data, specifically in the division at the 30 µm vesicle size. For bubbles >30 µm in diameter, growth by coalescence outstripped diffusion and decompression as the dominant growth mechanism.

Klug and Cashman (1994) argue for syneruptive vesiculation and syn- and posteruptive coalescence as the source of the polymodality seen in the vesicle size distributions of the Mount St. Helens pumices. Based on qualitative observations and the high fractal dimension, coalescence was clearly a significant syneruptive process for the Novarupta dacites, but no evidence has been found to suggest post-fragmentation modification of clast textures (e.g., Thomas et al. 1994; Gardner et al. 1996). The 1912 deposits contain pumices up to 50 cm in diameter, and careful field examination of rim-to-core textures shows no obvious shifts in bubble size or density from the clearly quenched exteriors into the interiors of the blocks.

Bubble collapse: maturation of texture

Quantitatively, clasts representing different phases of activity during episodes II and III are surprisingly similar. Trends on plots of population density and cumulative number density against bubble size show undeniable coincidence (Figs. 9 and 13). The most distinctive clast populations occur in Layer G and as such have been studied in greater detail because of the implications for the close of explosive volcanism. Samples from G show a sharp increase in mode and mean density compared to layers C–F (Figs. 4 and 5) reflecting comparatively thicker glass interstices and a smaller bubble population. From F to G, the melt changes from thinner glass walls and a bubble
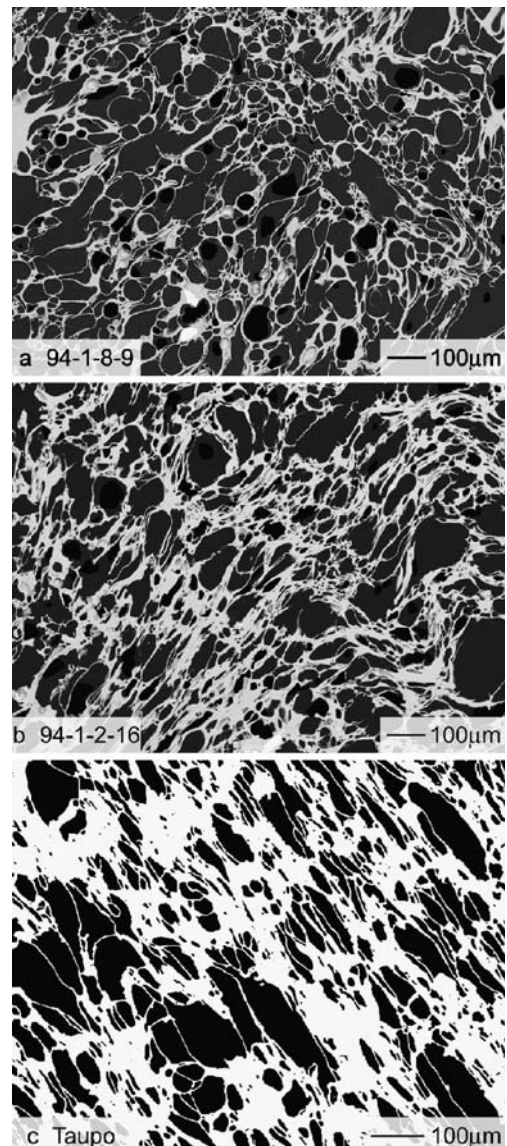

Fig. 14 Textures distinctly change from Layer F to Layer G preserving the onset of increased permeability in the melt and gas escape. **a** F-modal density clast with thin glass walls and a predominance of intermediate-sized bubbles. **b** G-modal density clast characterized by thicker glass walls, a larger population of small bubbles, and tear-shaped vesicles. **c**) Sample from Rotongaio ash in the 180 ka eruption of Taupo, New Zealand showing similar textures to Novarupta Layer G. In (**b**) and (**c**) textures are the result of bubble collapse and signify maturation of the melt

size distribution dominated by intermediate sizes (Fig. 14a) to thicker glass walls and a bubble size distribution skewed towards small sizes (Fig. 14b). Also conspicuous in Layer G is the increasingly pinched appearance of vesicles; the long diameter of elliptical vesicles often terminates in a tear or V-like shape. Similar textures characterize dome-related samples from the 1.8 ka Taupo eruption (Fig. 14c). We suggest the textural signatures seen in G pumices are created by the onset of bubble wall collapse. Collapse of a bubble would thicken glass interstices and inflict irregularities along the smooth, concave walls of nearby bubbles.

Discussion

Changing conduit processes imprinted microtextural variations among pyroclasts erupted throughout the Plinian activity at Novarupta. The dynamics of volatile exsolution and ascent governed the shapes and sizes of bubbles in the melt. Textural signatures were created by processes including (1) bubble nucleation, (2) growth by diffusion, decompression, and coalescence, and (3) collapse. All three processes were probably occurring simultaneously, but the significance of each varied in space and time.

Diversity within samples: heterogeneity in the conduit

If the melt represented by pumices collected at the same stratigraphic level entered the conduit at a single instant in time and followed identical paths up the conduit until fragmentation, the range in densities and textures should be narrow. The wide range of densities within the Novarupta samples for pyroclasts essentially fragmented and erupted at the same time might indicate instead that different degassing histories characterized different portions of the melt. Material that enters the conduit and ascends relatively slowly might be expected to have a more mature bubble texture than material with a shorter residence time in the conduit. Hence, the range of textures in pumices from a single stratigraphic level might represent the range of textural maturity induced by greater or lesser residence time in the conduit. This variation in residence time can be explained by variable ascent rates across the conduit. With continued eruption through a moderate-sized conduit, shear zones develop along the sides of the conduit and bound a non-shearing plug. Ascent of this plug is described by equal velocity bounded by narrow zones of sharply decreasing velocity proximal to the conduit walls (Cas and Wright 1987; Jaupart and Tait 1994; Dobran 2001). Plug flow in the conduit would ensure that melt traveling adjacent to the conduit wall had a longer residence time than melt occupying the center of the conduit. A similar explanation for textural heterogeneities found in Pinatubo 1991 pumice is offered by Polacci et al. (2001). Variations in velocity and shear across the width of the conduit create different ascent histories in terms of rates of bubble nucleation, growth, and collapse and thus variations in textures.

Based on the wide range in densities and the qualitative observations of the Layer G-modal density pumice compared to layers C-F, high and low-density clasts were also analyzed. While the general characteristics described for the modal density clasts hold for all clasts, a progression of textures is evident. Low-density G pumice (Fig. 8c) appear very similar to F pumice (Fig. 14a) whereas high-density G pumice show the thickest glass walls of all examined clasts and the most bubbles with complex shapes. We propose two possible explanations for the range of textures seen in Layer G. Firstly, modal density texture represents the least mature pumice. With continued coalescence and depletion of volatiles in the melt, dominant bubble size increases and walls thin producing low-density pumice. Eventually,

permeability reaches a critical level, gas escape reduces internal bubble pressure, and collapse occurs creating the high-density pumice. Secondly, low density texture marks the least mature pumice. Collapse is beginning to occur in modal density pumice but has become a more significant process in the high-density pumice. In either scenario, collapse occurs with continued degassing and marks an advanced state of maturation. Vesicle shape comparisons between clasts support the latter scenario. With maturity, coalescence produces increasingly more complex bubble shapes. In the high magnification images in Fig. 8, vesicles in the low-density clast are less amoeboid than their analogs in the modal and high-density clasts suggesting a lesser degree of maturity.

Diversity between samples: temporal changes
within an episode

While density and textural variations within an individual sample might be explained by the velocity profile across the conduit, melt vesiculation processes can be studied by comparing the modal density clasts through time, i.e., from each eruptive unit. Layer C represents sustained Plinian activity during Episode II, and D represents waning activity. Intermediate-sized bubbles dominate Layer C (Fig. 6d), but as Episode II continues, the size distribution becomes skewed towards larger vesicles (Layer D; Figs. 6c and 10). The coarsest bubbles and the thinnest walls of all the examined clasts characterize Layer D. Although the change in VVDs from C to D is slight (Fig. 10), the shift could reflect an increasing influence of bubble growth with respect to nucleation, i.e., growth by diffusion, decompression, and predominantly coalescence outstripping nucleation (Fig. 15). Progressive and unidirectional changes in the melt are more pronounced during Episode III. Bubble sizes are evenly spread around a peak of 80 μm for clasts from Layer F (94-1-8-9, 94-Z-2-4, 94-Z-14-3 in Fig. 10). Layer G clasts (94-1-2-16, 94-Z-22-24), representing the close of Episode III and the cessation of Plinian activity, are characterized by more abundant fine-intermediate bubble sizes and the thickest glass walls of the analyzed clasts (Figs. 8 and 14b). At 94-1, 71% by volume of the vesicles in the F clast are ≤0.12 mm in diameter whereas that amount rises to 80% in the G clast (94-1-2-16). The quantitative increase in small bubbles for the G clast perhaps signifies prolonged nucleation and comparatively less growth, but we do not favor this interpretation. The largest vesicles measured for G clasts (94-1-2-16 and 94-Z-22-24) are not significantly smaller than for layers C–F (Fig. 10). Furthermore, bubble shapes (Figs. 8 and 14b) and a power-law distribution for vesicles >30 μm (Fig. 13) suggest coalescence was still a dominant process during G-time. We believe the skewing towards finer vesicle sizes and the thickening of the glass walls for Layer G pumice were produced by collapse. Thus, the evolution of the melt from F to G favors bubble growth over nucleation and eventually the onset of bubble collapse (Fig. 15) and the advent of open-system behavior.

Pauses and breaks in the Novarupta eruption

The ends of episodes II and III mark the start of the two most significant breaks in the 1912 eruption. In both cases, Plinian volcanism ceased, but significant differences characterize the two events. The close of Episode III marked an end to sustained explosive volcanism, replaced by extrusion of partially outgassed magma and Vulcanian explosions during Episode IV. The break between episodes II and III ended with a blast-like vent-clearing pyroclastic density current (PDC 4 of Houghton et al. 2004) followed by the resumption of vigorous Plinian activity (Fig. 1). The deposits of PDC 4 show the most radial distribution of any of the PDC deposits described in Houghton et al. (2004) and are rich in wall-rock lithic clasts. The lithic population is conspicuously rich in vitrophyre clasts derived from Episode I deposits which formed the vent walls during Episode II. PDC 4 is also rich in pink-oxidized and perlitized rhyolite clasts which we suspect but cannot prove are recycled from the Episode I deposits. Important differences in the microtextures of the dacite erupted immediately prior to the two breaks are also evident. Vesicularity does not change significantly with time through Episode II although Layer D pumices do show a higher degree of bubble coalescence with thin glass walls and a high content of large vesicles with respect to Layer C (Fig. 6c, d). In contrast, throughout Episode III both the mean and maximum density of pumices shift; the increase becomes progressively more marked during the accumulation of Layer G (Figs. 4 and 5). Image analyses show that
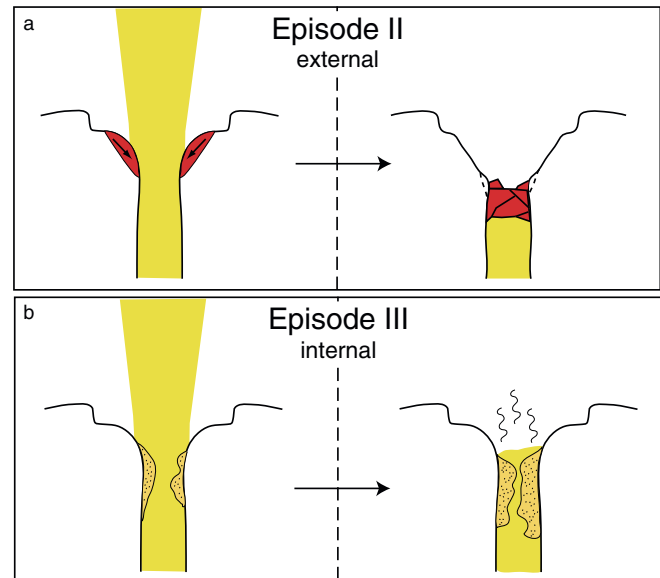
Fig. 16 Cartoon illustrating changes to the vent marking the close of Plinian episodes II and III. **a** External processes, probably instability of vent walls, created a blockage and temporarily shut down the eruption during Episode II. **b** For Episode III, internal changes led to the cessation of Plinian activity; maturation of melt allowed free escape of gas. Accumulation of outgassed melt eventually blocked the conduit and was followed by periods of dome growth

this shift is produced by a decrease in bubble size and an increase in the average thickness of bubble walls (Figs. 6a, b, 8b and 14a, b).

The contrasts suggest two different mechanisms operated to terminate Plinian episodes II and III. Textural evidence does not support a degassing-driven pause between episodes II and III. Instead, we propose that a short-lived blockage of the conduit, perhaps following collapse of the vent walls or shallow conduit, caused this break (Fig. 16a). The initiation of Episode III by the blast-like PDC carrying lithologies typical of the shallow walls of the Episode II vent supports this mechanism. In contrast, the close of Episode III and the permanent shift to effusive volcanism is marked by the first appearance of bubble collapse in turn reflecting the development of permeability in the melt and the onset of partial open-system degassing (Fig. 16b).

Conclusions

Plinian/ignimbrite activity stopped briefly and abruptly twice during the Novarupta 1912 eruption before the eruption style changed to effusive. The pause after 45 h and the termination after 60 h appear to have different causes. The shift to effusive volcanism at Novarupta, as for other historical high intensity eruptions, was driven by a change to open-system degassing and slow ascent of magma within the conduit and appears to be independent of any external changes to the conduit and vent. Our data show that such shifts in eruption regime, even if they occur
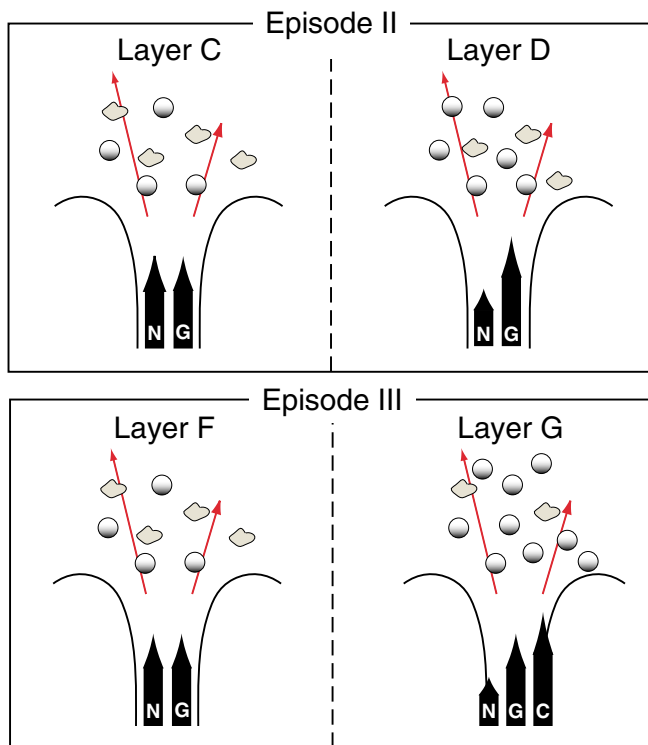

Fig. 15 Cartoon illustrating evolution of conduit processes with time based on textural evidence. Size of arrows indicates relative significance of nucleation (*N*), growth (*G*), and collapse (*C*)

suddenly, can be heralded by changes in the microtextures of the Plinian pumices. In contrast, no dramatic shift in magma rheology or ascent dynamics preceded the pause between episodes II and III. External change–probably minor vent wall collapse subsequently cleared by a blast-like explosion at the initiation of Episode III–instead drove the stay in activity.

References

Blower JD, Keating JP, Mader HM, Phillips JC (2001a) Inferring volcanic degassing processes from vesicle size distributions. Geophys Res Lett 28:347–350

Blower JD, Mader HM, Wilson SDR (2001b) Coupling of viscous and diffusive controls on bubble growth during explosive volcanic eruptions. Earth Planet Sci Lett 193:47–56

Blower JD, Keating JP, Mader HM, Phillips JC (2002) The evolution of bubble size distributions in volcanic eruptions. J Volcanol Geotherm Res 120:1–23

Bursik MI, Woods AW (1991) Buoyant, superbuoyant and collapsing eruption columns. J Volcanol Geotherm Res 45:347–350

Bursik MI, Carey SN, Sparks RSJ (1992) A gravity current model for the May 18, 1980 Mount St. Helens plume. Geophys Res Lett 19:1663–1666

Carey S, Sparks RSJ (1986) Quantitative models of the fallout and dispersal of tephra from volcanic eruption columns. Bull Volcanol 48:109–125

Carey S, Sigurdsson H (1989) The intensity of Plinian eruptions. Bull Volcanol 51:28–40

Carey S, Sigurdsson H, Gardner JE, Criswell W (1990) Variations in column height and magma discharge during the May 18, 1980 eruption of Mount St Helens. J Volcanol Geotherm Res 43:99–112

Cas RAF, Wright JV (1987) Volcanic successions: modern and ancient. Allen and Unwin, London, pp 1–528

Cashman KV (1992) Groundmass crystallization of Mount St Helens dacite, 1980–1986-a tool for interpreting shallow magmatic processes. Contrib Mineral Petrol 109:431–449

Cashman KV, Marsh BD (1988) Crystal size distribution (CSD) in rocks and the kinetics and dynamics of crystallization. II. Makaopuhi Lava Lake. Contrib Mineral Petrol 99:292–305

Cashman KV, Mangan MT (1994) Physical aspects of magmatic degassing. II. Constraints on vesiculation processes from textural studies of eruptive products. In: Carroll MR, Holloway JR (eds) Volatiles in Magmas. Rev Mineral 30:447–478

Cashman KV, Sturtevant B, Papale P, Navon O (2000) Magmatic fragmentation. In: Sigurdsson H (ed) Encyclopedia of volcanoes. Academic Press, San Diego, pp 421–430

Cioni R, Santacroce R, Sbrana A (1999) Pyroclastic deposits as a guide for reconstructing the multi-stage evolution of the Somma-Vesuvius Caldera. Bull Volcanol 61:207–222

Coombs ML, Gardner JE (2001) Shallow-storage conditions for the rhyolite of the 1912 eruption at Novarupta, Alaska. Geol Soc Am Bull 29:775–778

Curtis GH (1968) The stratigraphy of the ejecta of the 1912 eruption of Mount Katmai and Novarupta, Alaska. Geol Soc Am Bull 72:153–210

Dobran F (2001) Volcanic Processes: Mechanisms in Material Transport. Kluwer/Plenum, New York, pp 1–618

Druitt TH, Young SR, Baptie B, Bonadonna C, Calder ES, Clarke AB, Cole PD, Harford CL, Herd RA, Luckett R, Ryan G, Voight B (2002) Episodes of cyclic Vulcanian explosive activity with fountain collapse at Soufrière Hills Volcano, Montserrat. In: Druitt TH, Kokelaar BP (eds) The eruption of Soufrière Hills volcano, Montserrat, from 1995 to 1999. Geol Soc London Mem 21:281–306

Ernst GGJ, Sparks RSJ, Carey SN, Bursik MI (1996) Sedimentation from turbulent jets and plumes. J Geophys Res 101:5575–5589

Fierstein J, Hildreth W (1992) The plinian eruptions of 1912 at Novarupta, Katmai National Park, Alaska. Bull Volcanol 54:646–684

Francis P (1993) Volcanoes: a planetary perspective. Oxford University Press, New York, pp 1–443

Gaonac'h H, Lovejoy S, Stix J, Scherzter D (1996a) A scaling growth model for bubbles in basaltic lava flows. Earth Planet Sci Lett 139:395–409

Gaonac'h H, Stix J, Lovejoy S (1996b) Scaling effects on vesicle shape, size and heterogeneity of lavas from Mount Etna. J Volcanol Geotherm Res 74:131–153

Gardner JE, Thomas RME, Jaupart C, Tait S (1996) Fragmentation of magma during Plinian volcanic eruptions. Bull Volcanol 58:144–162

Gardner JE, Hilton M, Carroll MR (1999) Experimental constraints on degassing of magma: isothermal bubble growth during continuous decompression from high pressure. Earth Planet Sci Lett 168:201–218

Gurioli L, Houghton B, Cashman K, Cioni R (2004) Complex changes in eruption dynamics during the 79 AD eruption of Vesuvius. Bull Volcanol 67:144–159

Hammer JE, Cashman KV, Hoblitt RP, Newman S (1999) Degassing and microlite crystallization during pre-climactic events of the 1991 eruption of Mt. Pinatubo, Philippines. Bull Volcanol 60:355–380

Hammer JE, Rutherford MJ, Hildreth W (2002) Magma storage prior to the 1912 eruption at Novarupta, Alaska. Contrib Mineral Petrol 144:144–162

Hess KU, Dingwell DB (1996) Viscosities of hydrous leucogranitic melts: a non-Arrhenian model. Am Mineral 81:1297–1300

Hildreth W (1983) The compositionally zoned eruption of 1912 in the Valley of Ten Thousand Smokes, Katmai National Park, Alaska. J Volcanol Geotherm Res 18:1–56

Hildreth W (1987) New perspectives on the eruption of 1912 in the Valley of Ten Thousand Smokes, Katmai National Park, Alaska. Bull Volcanol 49:680–693

Hildreth W (1991) The timing of caldera collapse at Mount Katmai in response to magma withdrawal towards Novarupta. Geophys Res Lett 18:1541–1544

Hildreth W, Fierstein J (2000) Katmai volcanic cluster and the great eruption of 1912. Geol Soci Am Bull 112:1594–1620

Houghton BF, Wilson CJN (1989) A vesicularity index for pyroclastic deposits. Bull Volcanol 51:451–462

Houghton BF, Hobden BJ, Cashman KV, Wilson CJN, Smith RT (2003) Large-scale interaction of lake water and rhyolitic magma during the 1.8 ka Taupo eruption, New Zealand. In: White JDL, Smellie JL, Clague DA (eds) Explosive subaqueous volcanism. Geophys Monograph 140:97–109

Houghton BF, Wilson CJN, Fierstein J, Hildreth W (2004) Complex proximal deposition during the Plinian eruptions of 1912 at Novarupta, Alaska. Bull Volcanol 66:95–133

Hurwitz S, Navon O (1994) Bubble nucleation in rhyolite melts: experiments at high pressure, temperature, and water content. Earth Planet Sci Lett 122:267–280

Jaupart C, Allegre CJ (1991) Gas content, eruption rate and instabilities of eruption regime in silicic volcanoes. Earth Planet Sci Lett 102:413–429

Jaupart C, Tait S (1994) Dynamics of eruptive phenomena. In: Carroll MR, Holloway JR (eds) Volatiles in magmas. Rev Mineral 30:213–238

Klug C, Cashman KV (1994) Vesiculation of May 18, 1980, Mount St. Helens magma. Geology 22:468–472

Klug C, Cashman KV (1996) Permeability development in vesiculating magmas: implications for fragmentation. Bull Volcanol 58:87–100

Klug C, Cashman KV, Bacon CR (2002) Structure and physical characteristics of pumice from the climactic eruption of Mount Mazama (Crater Lake), Oregon. Bull Volcanol 64:486–501

Kokelaar BP (2002) Setting, chronology and consequences of the eruption of Soufrière Hills Volcano, Montserrat (1995–1999). In: Druitt TH, Kokelaar BP (eds) The eruption of Soufrière Hills volcano, Montserrat, from 1995 to 1999. Geol Soc London Mem 21:1–43

Koyaguchi T (1994) Grain-sized variation of tephra derived from volcanic umbrella clouds. Bull Volcanol 56:1–9

Lowenstern JB (1993) Evidence for a copper-bearing fluid in magma erupted at the Valley of Ten Thousand Smokes, Alaska. Contrib Mineral Petrol 114:409–421

Lyakhovsky V, Hurwitz S, Navon O (1996) Bubble growth in rhyolitic melts: experimental and numerical investigation. Bull Volcanol 58:19–32

Manga M, Castro J, Cashman KV, Loewenberg M (1998) Rheology of bubble-bearing magmas. J Volcanol Geotherm Res 87:15–28

Mangan MT, Cashman KV (1996) The structure of basaltic scoria and reticulite and inferences for vesiculation, foam formation, and fragmentation in lava fountains. J Volcanol Geotherm Res 73:1–18

Mangan MT, Sisson T (2000) Delayed, disequilibrium degassing in rhyolite magma: decompression experiments and implications for explosive volcanism. Earth Planet Sci Lett 183:441–455

Mangan MT, Cashman KV, Newman S (1993) Vesiculation of basaltic magma during eruption. Geology 21:157–160

Mangan MT, Mastin L, Sisson T (2004) Gas evolution in eruptive conduits: combining insights from high temperature and pressure decompression experiments with steady-state flow modeling. J Volcanol Geotherm Res 129:23–36

Marsh BD (1988) Crystal size distribution (CSD) in rocks and the kinetics and dynamics of crystallization. I. Theory. Contrib Mineral Petrol 99:277–291

Marti J, Soriano C, Dingwell DB (1999) Tube pumices as strain markers of the ductile-brittle transition during magma fragmentation. Nature 402:650–653

Melnik O (2000) Dynamics of two-phase conduit flow of high-viscosity gas-saturated magma: large variations of sustained explosive eruption intensity. Bull Volcanol 62:153–170

Mourtada-Bonnefoi CC, Laporte D (1999) Experimental study of homogenous bubble nucleation in rhyolitic magmas. Geophys Res Lett 26:3505–3508

Navon O, Lyakhovsky V (1998) Vesiculation processes in silicic magmas. In: Gilbert GS, Sparks RSJ (eds) Geol Soc Spec Publ 145:27–50

Orsi G, Gallo G, Heiken G, Wohletz K, Yu E, Bonani G (1992) A comprehensive study of pumice formation and dispersal: the Cretaio tephra of Ischia (Italy). J Volcanol Geotherm Res 53:329–354

Paladio-Melosantos ML, Solidum R, Scott WE, Quimbao RB, Umbal JV, Rodolfo KS, Tubianosa BS, Delos Reyes PJ (1995) Tephra falls of the 1991 eruptions of Mount Pinatubo. In: Newhall CGP, Punongbayan RS (eds) Fire and mud: eruptions and lahars of Mount Pinatubo. Washington Press, Philippines, pp 513–535

Pinkerton H, Stevenson RJ (1992) Methods of determining the rheological properties of magmas at sub-liquidus temperatures. J Volcanol Geotherm Res 53:47–66

Polacci M, Papale P, Rosi M (2001) Textural heterogeneities in pumices from the climactic eruptions of Mount Pinatubo, 15 June 1991, and implications for magma ascent dynamics. Bull Volcanol 63:83–97

Polacci M, Pioli L, Rosi M (2003) The Plinian phase of the Campanian Ignimbrite eruption (Phlegrean Fields, Italy): evidence from density measurements and textural characterization of pumice. Bull Volcanol 65:418–432

Proussevitch AA, Sahagian DL (1996) Dynamics of coupled diffusive and decompressive bubble growth in magmatic systems. J Geophys Res 101:17447–17455

Proussevitch AA, Sahagian DL (1998) Dynamics and energetics of bubble growth in magmas: analytical formulation and numerical modeling. J Geophys Res 103:18223–18251

Proussevitch AA, Sahagian DL, Kutolin VA (1993) Stability of foams in silicate melts. J Volcanol Geotherm Res 59:161–178

Pyle DM (1989) The thickness, volume and grain-size of tephra fall deposits. Bull Volcanol 51:1–15

Rosi M, Paladio-Melosantos ML, Dimuro A, Leoni R, Bacolcol T (2001) Fall vs flow activity during the 1991 climactic eruption of Pinatubo Volcano (Philippines). Bull Volcanol 62:549–566

Rust AC, Manga M, Cashman KV (2003) Determining flow type, shear rate and shear stress in magmas from bubble shapes and orientations. J Volcanol Geotherm Res 122:111–132

Sahagian DL, Proussevitch AA (1998) 3D particle size distributions from 2D observations: stereology for natural applications. J Volcanol Geotherm Res 84:173–196

Self S (1992) Krakatau revisited: the course of events and interpretation of the 1883 eruption. GeoJournal 28:109–121

Self S, Rampino MR (1981) The 1883 eruption of Krakatau. Nature 294:699–704

Sigurdsson H, Carey SN, Espindola JM (1984) The 1982 eruptions of El Chichon volcano, Mexico: stratigraphy of pyroclastic deposits. J Volcanol Geotherm Res 23:11–37

Simakin A, Armienti P, Epel'baum M (1999) Coupled degassing and crystallization: experimental study at continuous pressure drop with application to volcanic bombs. Bull Volcanol 61:275–287

Sparks RSJ (1986) The dimensions and dynamics of volcanic eruption columns. Bull Volcanol 48:3–15

Sparks RSJ, Brazier S (1982) New evidence for degassing processes during explosive eruptions. Nature 295:218–220

Sparks RSJ, Bursik MI, Ablay GJ, Thomas RME, Carey SN (1992) Sedimentation of tephra by volcanic plumes. II. Controls on thickness and grain-size variations of tephra fall deposits. Bull Volcanol 54:685–695

Sparks RSJ, Bursik MI, Carey SN, Gilbert JS, Glaze LS, Sigurdsson H, Woods AW (1997) Volcanic plumes. Wiley, Chichester, pp 1–574

Spera FJ (2000) Physical properties of magma. In: Sigurdsson H (ed) Encyclopedia of Volcanoes. Academic Press, San Diego pp 171–190

Thomas N, Jaupart C, Vergniolle S (1994) On the vesicularity of pumice. J Geophys Res 99:15,633–15,644

Toramaru A (1988) Formation of propagation pattern in two-phase flow systems with application to volcanic eruptions. Geophys J 95:613–623

Toramaru A (1989) Vesiculation process and bubble size distributions in ascending magmas with constant velocities. J Geophys Res 94:17523–17542

Toramaru A (1990) Measurement of bubble size distributions in vesiculated rocks with implications for quantitative estimation of eruptive processes. J Volcanol Geotherm Res 43:71–90

Walker GPL (1973) Explosive volcanic eruptions: a new classification scheme. Geol Rundsch 62:431–446

Whitham A, Sparks R (1986) Pumice. Bull Volcanol 48:209–223

Wilson CJN, Walker GPL (1985) The Taupo eruption, New Zealand. I. General aspects. Philos Trans R Soc Lond A314:199–228

Wilson L, Sparks RSJ, Walker GPL (1980) Explosive volcanic eruptions-IV. The control of magma properties and conduit geometry on eruption column behaviour. Geophys J R Astr Soc 63:117–148

Wilson L, Walker GPL (1987) Explosive volcanic eruptions-VI. Ejecta dispersal in plinian eruptions: the control of eruption conditions and atmospheric properties. Geophys J R Astr Soc 89:657–679

Woods AW (1988) The fluid-dynamics and thermodynamics of eruption columns. Bull Volcanol 50:169–193

Woods AW, Bower SM (1995) The decompression of volcanic jets in a crater during explosive volcanic eruptions. Earth Planet Sci Lett 131:189–205